Glycosylated IgG antibodies contribute to the recovery of haemorrhagic fever with renal syndrome patients

Chuansong Quan[1,2,3†], Lu Wang[3,4†], Jiming Gao[5†], Yaoni Li[6†], Xiaoyu Xu[7†], Houqiang Li[3], Zixuan Gao[7], Wenxu Ruan[7], Hongzhi Liu[3], Qian Li[3], Weijia Xing[3], Liqiong Zhao[6], Michael J. Carr[8,9], Weifeng Shi[10,11*], Haifeng Hou[3*]

[1]Key Laboratory of Emerging Infectious Diseases in Universities of Shandong, Shandong First Medical University & Shandong Academy of Medical Sciences, Ji'nan, 250117, China

[2]The Second Affiliated Hospital of Shandong First Medical University, Taian, 271000, China

[3]School of Public Health, Shandong First Medical University & Shandong Academy of Medical Sciences, Ji'nan, 250117, China

[4]Medical Records and Statistics Management Office, Tengzhou Central People's Hospital, Zaozhuang, 277500, China

[5]Department of Neurobiology and Physiology, School of Clinical and Basic Medicine, Shandong First Medical University& Shandong Academy of Medical Sciences, Ji'nan, 250117, China

[6]Baoji Central Hospital, Baoji, 721008, China

[7]School of Life Sciences, Shandong First Medical University & Shandong Academy of Medical Sciences, Taian, 271016, China.

[8]National Virus Reference Laboratory, School of Medicine, University College Dublin, D04 E1W1, Ireland.

[9]International Collaboration Unit, International Institute for Zoonosis Control, Hokkaido University, N20 W10 Kita-ku, Sapporo 001-0020, Japan.

[10]Ruijin Hospital, Shanghai Jiao Tong University School of Medicine, Shanghai, 200025, China.

[11]Shanghai Institute of Virology, Shanghai Jiao Tong University School of Medicine, Shanghai, 200025, China

*Correspondence:

Haifeng Hou: hfhou@sdfmu.edu.cn

Weifeng Shi: shiwf@ioz.ac.cn

†These authors contributed equally to this work

Abstract

Haemorrhagic fever with renal syndrome (HFRS) is a fatal disease caused by Hantaan virus (HTNV) infection. Humoral immunity is essential for effective viral clearance, however, the glycosylation characteristics of immunoglobulin G (IgG) in HFRS patients is not well known. Peripheral blood mononuclear cells from HFRS patients were obtained for B subset analysis using scRNA-seq and flow cytometry. HTNV specific IgG antibody titers were detected by enzyme-linked immunosorbent assay, and IgG glycosylation was analyzed by ultra-performance liquid chromatography. The proportions of the antibody-secreting memory (ASM) B cells and plasmablasts (PB) were significantly expanded among acute HFRS patients. We discovered significantly increased fucosylated IgG and decreased bisecting N-acetylglucosamine during the convalescent phase of HTNV infection. Meanwhile, positive correlations were observed between ASM subsets and galactosylation/sialylation in the IgG Fc region, and between PB subsets and sialylation. Notably, the glycosylation-related genes, such as *RPN1 and RPN2*, were primarily expressed differentially in the ASM and PB subclusters which were enriched in the N-glycosylation modifications of proteins through asparagine. Our findings indicated that IgG N-glycosylation may play a crucial role in combating HTNV infection and contributing to clinical recovery, which provided new insights for optimizing glycoengineered therapeutic antibodies.

Keywords: Haemorrhagic fever with renal syndrome (HFRS); Hantaan virus (HTNV); B cell; Immunoglobulin G (IgG); Glycosylation; Inflammation

58 **Introduction**

59 The causative agent of haemorrhagic fever with renal syndrome (HFRS) is Hantaan
60 virus, which belongs to the family *Hantaviridae* and is primarily transmitted by rodents
61 (Zheng et al., 2019). China is the most heavily affected country by HFRS, accounting
62 for >90% of global cases, and a total of 32,462 cases of HFRS were reported in China
63 during 2019–2022, with a fatality rate ranging from 0.1 to 15% (R. Li et al., 2023)
64 (https://www.chinacdc.cn).

65 Hantaviruses are tri-segmented, single-stranded, negative-sense RNA viruses, whose
66 genomes consist of three regions: large (L), medium (M), and small (S). The
67 glycoproteins Gn and Gc, encoded by the M segment, can infect target cells - primarily
68 vascular endothelial cells - via β3 integrin receptors (Pizarro et al., 2019).
69 Simultaneously, they could also infect other cell types, such as mononuclear
70 macrophages and dendritic cells, leading to systemic viral infection. Although
71 hantavirus replication is thought to occur primarily in the vascular endothelium without
72 direct cytopathic effects, a plethora of innate immune cells mediate host antiviral
73 defenses. These include natural killer cells, neutrophils, monocytes, and macrophages,
74 together with pattern recognition receptors (PRRs), interferons (IFNs), antiviral
75 proteins, and complement activation, e.g., via the pentraxin 3 (PTX3) pathway, which
76 can exacerbate HFRS disease progression leading to immunopathological damage
77 through cytokine/chemokine production, cytoskeletal rearrangements in endothelial
78 cells, ultimately amplifying vascular dysfunction (Tariq & Kim, 2022). Rapid and
79 effective humoral immune responses, however, such as neutralizing antibody responses
80 targeting the glycoproteins Gn/Gc, contribute to rapid recovery from HFRS and are
81 critical for protection from severe disease (Engdahl & Crowe, 2020; Li et al., 2020).

82 Immunoglobulin G (IgG) N-linked glycosylation mediates critical functions

83 modulating antiviral immunity during viral infection. Changes in the conserved N-
84 linked glycan Asn297 in the Fc region of IgG typically by fucosylation, galactosylation,
85 or sialylation can alter antibody effector function. A reduction in core fucosylation
86 decreases IgG binding to NK cell FcγRIIIa promotes antibody-dependent cellular
87 cytotoxicity (ADCC) necessary for clearance of viruses, including SARS-CoV-2,
88 dengue and HIV-1 whereas sialylation can attenuate immune responses resulting in
89 immune evasion (Ash et al., 2022; Haslund-Gourley et al., 2024; Hou et al., 2021; Wang
90 et al., 2017). Changes in IgG and other protein N-linked glycosylation profiles therefore
91 shape virus-host interactions and disease progression.

92 Importantly, there have not been prior studies specifically examining plasma IgG N-
93 glycome profiles derived from chromatographic peak data in HFRS patients,
94 particularly in relation to seroconversion status. This gap in our knowledge motivated
95 our systematic investigation of both total and virus-specific IgG glycosylation
96 dynamics during acute infection. In the present study, we combined scRNA-seq and
97 flow cytometry to reveal the phenotypes of B cell responses during Hantaan virus
98 (HTNV) infection, and explored the transcriptomic features of reactive B cell subsets.
99 A total of 166 HFRS patients, including 65 paired HFRS samples, were employed to
100 profile the IgG-Fc glycosylation pattern and to investigate the potential regulatory role
101 of IgG-Fc glycosylation in HFRS pathogenesis.

102 **Results**

103 **B cell compositional characteristics in HFRS patients**

104 To characterize the humoral immune profiles in HFRS patients, we enrolled 166
105 suspected HTNV-infected patients who were admitted to Baoji Central Hospital in
106 Shaanxi Province, China, between October 2019 and January 2022. Among them, 65
107 met the inclusion criteria and were included in the study (Figure 1). We identified a

108 total of eight cell subpopulations, including subsets of CD4 T cells, CD8 T cells, CD14
109 monocytes, NK cells, B cells, platelets, endothelial progenitor cells, and red blood cells
110 (Figure 2—figure supplement 1A and B). The proportions of these cell types were
111 comparable between acute HFRS patients and healthy controls, with no significant
112 batch effects observed (Figure 2—figure supplement 1C). CD4 T cells (31.4%) were
113 the predominant subset prior to HTNV infection, whereas CD8 T cells (44%) became
114 the dominant population post-infection. Notably, the proportions of NK cells (15.9% to
115 5.6%, $p<0.001$) and platelets (3.1% to 0.6%, $p<0.01$) significantly decreased, whereas
116 the level of CD14 monocytes (15.9% to 32.3%, $p<0.05$) nearly doubled. The overall
117 proportions of B cells, however, did not exhibit significant changes (Figure 2—figure
118 supplement 1D and E).

119 To precisely elucidate the role of B cell subsets in anti-HTNV infection, we classified
120 B cells into eight subsets, including antibody-secreting memory B cells (ASM), double-
121 negative B cells (DN), intermediate memory B cells (IM), marginal zone-like B cells
122 (MZB), naive B cells (naive B), plasmablasts (PB), quiescent resting memory B cells
123 (RM), and exhausted tissue-like memory B cells (TLM) (Figure 2A and B, and Figure
124 2—figure supplement 1F). We discovered that significant expansion of ASM, PB, and
125 RM cell populations in acute HFRS patients compared to healthy controls,
126 accompanied by contraction of DN, IM, and naive B cell compartments post-infection
127 (Figure 2C). In healthy controls, naive B cells (42.87%), DN B cells (26.65%), and
128 TLM B cells (16.13%) constituted the majority of the B cell population. However, ASM
129 (30.96%), PB cells (11.12%) and RM B cells (2.88%), became the dominant subsets
130 after HTNV infection (Figure 2D and Supplementary file 1).

131 To validate the accuracy of our single-cell subpopulation analysis, we employed flow
132 cytometry to quantify the B cell subsets in acute and convalescent HFRS patients

133 (Figure 2E). The results demonstrated that ASM (39.48% vs. 24.57%, p<0.001) and PB
134 (23.97% vs. 2.61%, p <0.001) subsets were significantly amplified in the acute phase
135 compared to the convalescent phase (Figure 2F). Conversely, the number of naive B
136 cells (32.78% vs. 48.92%, p=0.003) and CSM cells (18.65% vs. 27.15%, p=0.008)
137 recovered rapidly in the convalescent stage (Figure 2F), consistent with the
138 observations at the transcriptome level. No significant differences were observed for
139 other B cell subtypes between the acute and convalescent stages (Figure 2—figure
140 supplement 2). These results demonstrated that several B cell subpopulations were
141 effectively activated following HTNV infection.

142 **Dynamic characteristics of the IgG N-glycome in HFRS patients**

143 HFRS patients were further stratified into three age groups (≤44, 45-59, and ≥60
144 years). IgG glycosylation was analyzed by ultra-performance liquid chromatography.
145 As shown in Supplementary file 2, no significant differences in IgG glycosylation were
146 observed between age groups, except for galactosylation (p=0.001). Similarly, no sex-
147 based differences in IgG-Fc glycosylation were noted (Supplementary file 3). However,
148 the levels of IgG with bisecting GlcNAc (15.72% vs. 14.51%, p<0.001), galactosylated
149 IgG (74.26% vs. 71.15%, p<0.001), and sialylated IgG (22.44% vs. 21.62%, p<0.001)
150 were significantly higher in the acute phase compared to the convalescent phase.
151 Conversely, fucosylated IgG levels (94.29% vs. 94.89%, p<0.001) were lower in the
152 acute phase (Supplementary file 4), indicating that IgG N-glycosylation plays a critical
153 role in the anti-infection process. Multivariate linear regression was employed to
154 mitigate potential confounding by genetic and environmental factors in the glycomics
155 analysis. While no significant associations were observed for most glycan models
156 (fucosylation, p=0.526; bisecting GlcNAc, p=0.069; and sialylation, p=0.058), we
157 discovered sex showed a potentially influential effect on galactosylation (p=0.001)

158 (Supplementary files 5-8). These results suggest that while most glycan features appear
159 unaffected by the examined covariates, galactosylation may be subject to sex-specific
160 biological regulation.

161 Among the 130 paired blood samples from 65 patients, 38 (29.2%) were negative for
162 HTNV nucleocapsid protein-specific IgG antibodies, and 92 (70.8%) were seropositive.
163 For the 24 patients with both seronegative and seropositive samples, levels of bisecting
164 GlcNAc (16.16% vs. 14.54%, p<0.001), galactosylation (74.12% vs. 70.94%, p=0.006),
165 and sialylation (22.92% vs. 21.80%, p=0.008) were higher in the seronegative period,
166 whereas that of fucosylation was lower (94.36% vs. 94.74%, p= 0.024) in this period
167 (Figure 3A). Notably, bisecting GlcNAc and sialylated IgG levels decreased as HTNV
168 nucleocapsid protein (NP)-specific antibody titers increased (Figure 3B), highlighting
169 a potential link between antibody levels and IgG-Fc glycosylation.

170 **The IgG N-glycome in HFRS patients with seroconversion**

171 A four-fold or greater increase in HTNV NP-specific antibody titers usually indicates
172 a protective humoral immune response during the acute phase (Onwuchekwa et al.,
173 2023). We observed a significant increase in the Fc fucosylation (94.18% vs. 94.48%,
174 p=0.044) and a decrease in bisecting GlcNAc (16.41% vs. 14.71%, p=0.001) post the
175 four-fold antibody titer increase compared to the baseline. However, no significant
176 differences were observed in galactosylation and sialylation (Figure 3C), suggesting
177 that fucosylation and bisecting GlcNAc may play key roles in anti-HTNV infection and
178 recovery.

179 **The potential source of the IgG N-glycome during HTNV infection**

180 Positive correlations were observed between the ASM subsets and both
181 galactosylation (p=0.017, r_s=0.418) and sialylation (p=0.008, r_s=0.458) in the antibody
182 Fc region, as well as between the PB subsets and sialylation (p=0.036, r_s=0.372) (Figure

183 4A-C). Therefore, we speculated that galactosylated antibodies may primarily originate
184 from the ASM subsets, while sialylated antibodies may derive from the ASM and PB
185 subsets.

186 To investigate the process of glycosylated antibody production secreted by the ASM
187 and PB subsets, we identified differentially expressed genes (DEGs) among the eight
188 B cell subpopulations. Notably, the most DEGs were observed in the ASM (470), naive
189 (312), and TLM (333) B subpopulations, respectively (Figure 4—figure supplement 1A
190 and Supplementary file 9). Specifically, among all the upregulated genes, the
191 expressions of glycosylation-related, mitochondrial respiratory-related, and peptide
192 chain elongation-related genes among the ASM, PB, and RM populations were elevated
193 after HTNV infection, including *RPN2*, *MT-ND6*, and *RPS26* (Figure 4—figure
194 supplement 1B and Supplementary file 10). On the contrary, the upregulated genes in
195 the naive, DN, and IM populations were related to anti-inflammatory and
196 immunosuppressive effects, inhibition of the antioxidative function, response to
197 environmental stress, and B-cell growth and development, such as *TSC22D3*, *TXNIP*,
198 *DUSP1*, and *KLF6*, whereas the downregulated genes played an important role in the
199 inflammatory response, cell motility, and antigen presentation, including *LTB*, *ACTG1*,
200 and *HLA-DRB5* (Figure 4—figure supplement 1C and Supplementary file 11).

201 Unexpectedly, we observed significant changes in the expression of glycosylation-
202 related genes (GRGs) in the ASM, PB, and RM subclusters during HTNV infection
203 compared to healthy controls. *RPN1* and *RPN2* were prominently upregulated, which
204 encoded subunits of the oligosaccharyltransferase complex (Figure 4D). This implied
205 that the process of glycosylation during HTNV infection was rapidly activated among
206 the ASM and PB subclusters. In the ASM subcluster, the fold change of GRGs from all
207 four glycosylation modification-related genes, aside from *RPN1* and *RPN2*, was similar,

208 suggesting that ASM may undergo complex and diverse glycosylation modification
209 processes.

210 To enhance our understanding of the transcriptomic characteristics of GRG-high-
211 expressing PB and ASM subclusters, we conducted a comprehensive pathway
212 enrichment analysis and identified significant enrichment of pathways related to
213 glycosylation modifications, including the endoplasmic reticulum protein-containing
214 complex, rough endoplasmic reticulum, and protein N-linked glycosylation via
215 asparagine (Figure 4E). Additionally, gene sets associated with glycosylation
216 modifications showed positive regulation of these pathways (p=0.002, Figure 4F).
217 These results indicated that glycosylation modifications in the ASM, PB, and RM
218 subpopulations were dynamically regulated during the acute phase of HFRS, likely to
219 satisfy the amplified anti-HTNV antibody requirement and accelerate viral clearance.

220 **Discussion**

221 IgG glycosylation is a key regulator of inflammatory responses for infectious
222 diseases, acting as a molecular switch between anti-inflammatory and pro-
223 inflammatory effects upon antigenic challenge. One of the most significant findings of
224 the present study is the elevation in IgG fucosylation and reduction in bisecting GlcNAc
225 levels at the time of a four-fold increases in the HTNV NP-specific antibody titers.
226 Afucosylation is known to enhance antibody-dependent cellular cytotoxicity (ADCC)
227 by increasing the affinity of IgG-Fc for the FcγRIIIa receptor on NK cells, leading to
228 heightened production of inflammatory cytokines such as IL-1β, IL-6, IFN-γ, and TNF-
229 α (Larsen et al., 2021; Lu, Suscovich, Fortune, & Alter, 2018; Wieczorek, Braicu,
230 Oliveira-Ferrer, Sehouli, & Blanchard, 2020). Increase in bisecting GlcNAc linked to
231 Fc induces enhanced affinity for the FcγIIIa receptor and enhanced ADCC function of
232 the antibodies (Giron et al., 2020; Hou et al., 2021; Irvine & Alter, 2020). However,

233 rather than directly influencing the Fc receptor binding, this modification enhances
234 antibody functionality through afucosylation, which subsequently increases the binding
235 affinity to the FcgRIIIa receptor (Ackerman et al., 2018; Jennewein & Alter, 2017). Our
236 findings provide evidence that the dynamic alterations in glycosylation patterns,
237 characterized by increased fucosylation and decreased bisecting GlcNAc levels during
238 viral infection, are involved in disease pathogenesis and clinical recovery, suggesting
239 their dual utility as both diagnostic biomarkers and promising therapeutic targets.

240 We also observed elevated galactosylation levels in the acute phase compared to the
241 convalescent phase, a phenomenon also reported in SARS-CoV-2 infections but not in
242 chronic diseases and cancers (Hou et al., 2021; Liu et al., 2018). Increased
243 galactosylation may expand the distance between CH2 domains, exposing key amino
244 acids for FcγRIIIa binding and enhancing ADCC functions (Houde, Peng, Berkowitz,
245 & Engen, 2010). Simultaneously, the increase in the ASM subset, which positively
246 correlated with galactosylation, may reflect polyclonal activation of memory B cells
247 driven by pattern recognition receptors and cytokines, leading to the production of
248 galactosylated antibodies. Similarly, sialylation levels were higher in the acute patients,
249 potentially linked to the expansion of the ASM and PB subsets. In this study, the PB
250 subset was significantly elevated in the acute phase and positively correlated with
251 sialylation, suggesting that rapidly proliferating plasmablasts may contribute to the
252 secretion of sialylated antibodies; however, the mechanisms behind this require further
253 investigation.

254 Antibody-related glycogenes are significantly activated following Hantaan virus
255 infection. We noted that ribophorin I and II (RPN1 and RPN2) were significantly
256 upregulated in the ASM/IM/PB/RM subsets after Hantaan virus infection, which linked
257 the high mannose oligosaccharides with asparagine residues found in the Asn-X-

258 Ser/Thr consensus motif (Hwang et al., 2025). We speculate that they continuously
259 attach the synthesized glycan chains to the constant region of antibodies during
260 antibody synthesis. Similarly, fucosyltransferase 8 (FUT8) in the ASM subset,
261 catalyzing the alpha1-2, alpha1-3, and alpha1-4 fucose addition (Wang & Ravetch,
262 2019; Yang et al., 2015), was downregulated in the mRNA translation, and the levels of
263 fucosylated antibodies were naturally lower in the acute HFRS patients. Meanwhile,
264 the beta-1,4-galactosyltransferase (beta4GalT) gene expression was significantly
265 elevated in the ASM subpopulation during the acute phase, which also correlated with
266 increased levels of galactosylated antibodies in serum (Wang & Ravetch, 2019).
267 However, we did not observe significant upward changes in sialyltransferase mRNA
268 expression in the acute HFRS patients, similar with the finding from severe COVID-19
269 cohorts (Haslund-Gourley et al., 2024). The neuraminidase 1 (NEU1) gene is strikingly
270 upregulated and may potentially explain the decreased sialylation on the secreted
271 HTNV-specific IgG antibodies during convalescence. Overall, the glycosylation of
272 immunoglobulin G is regulated by a large network of B-cell glycogenes during HTNV
273 infection.

274 Despite establishing a well-characterized patient cohort and performing systematic
275 IgG glycosylation profiling based on HTNV NP antibody status, this study has several
276 noteworthy limitations. Most notably, while preliminary comparisons suggested similar
277 patterns between virus-specific and total IgG N-glycome, our total plasma IgG analysis
278 may have introduced confounding factors in the observed associations. This
279 methodological constraint could potentially affect the interpretation of certain disease-
280 specific glycosylation signatures.

281 Our findings demonstrate that the IgG-Fc glycosylation plays a pivotal role in HTNV
282 infection and rapid recovery. Fucosylated oligosaccharides and the absence of bisecting

283 GlcNAc are associated with favorable clinical outcomes. Importantly, specific B cell
284 subsets, particularly ASMs and PBs, upregulated the secretion of galactosylated and
285 sialylated antibodies, respectively. These findings would deepen our understanding of
286 antibody glycosylation in antivirus immunity and provide a foundation for future
287 studies aimed at optimizing glycoengineered therapeutic antibodies.

288 **Materials and Methods**

289 **Study participants**

290 Clinical specimens were collected from HFRS patients who were hospitalized in
291 Baoji Central Hospital between October 2019 and January 2022. Patients were
292 categorized into four clinical subtypes (mild, moderate, severe, and critical) based on
293 the diagnostic criteria for HFRS issued by the Ministry of Health (Ma et al., 2015). This
294 study was approved by the ethics committee of the Shandong First Medical University
295 & Shandong Academy of Medical Sciences (R201937). Written informed consent was
296 obtained from each participant or their guardians.

297 The clinical course of HFRS is grouped into acute (febrile, hypotensive, and oliguric
298 stages) and convalescent (diuretic and convalescent stages) phases. The acute phase
299 was defined as within 12 days of illness onset, and the convalescent phase was defined
300 as a period of illness lasting 13 days or longer (Tang et al., 2019; Zhang et al., 2022).
301 The earliest sample was selected if there were multiple blood samples available in the
302 acute phase and the last available sample before discharge was selected if there were
303 multiple blood samples in the convalescent phase.

304 **Single-Cell RNA Sequencing and public database**

305 Flow cytometry antibody staining was conducted as previously described
306 (Chakraborty et al., 2022). Dead cell and red blood cell were removed using the BD
307 FACSAria™ III cell sorter, and peripheral blood mononuclear cells (PBMCs) were

308 collected for single-cell sequencing. The library construction was conducted as
309 previously described (Jin et al., 2024).

310 We obtained single-cell transcriptome sequencing data from the Gene Expression
311 Omnibus (GEO) database (GSE161354), containing six HFRS patients and two healthy
312 volunteers, as well as healthy control samples from the Genome Sequence Archive
313 (GSA) database (HRA000203), matched with patient demographic information.

314 **Single-Cell Data Analysis**

315 The FastQC software was used to evaluate the data obtained to ensure the quality of
316 the raw sequencing data. The raw data were mapped to the human reference genome
317 (GRCh38, https://cf.10xgenomics.com/supp/cell-exp/refdata-gex-GRCh38-2020-A.tar.
318 gz) using Cell Ranger. The Seurat R package (Version 4.4.0) was utilized for the
319 merging and clustering of single-cell data. The Harmony R package and the anchor
320 module of Seurat were used to remove batch effects between samples and groups for
321 cell clustering. t-distributed Stochastic Neighbor Embedding (t-SNE) and Uniform
322 Manifold Approximation and Projection (UMAP) were employed for dimensionality
323 reduction and visualization of individual cells.

324 **Cell Type Annotation**

325 UMAP and t-SNE were used to reduce the dimension of all cells and to cluster them
326 in a two-dimensional space based on shared features. The Single R (Version 2.2.0)
327 package was used to infer independently the cell origin of each single cell based on a
328 reference transcriptome dataset of pure cell types, for unbiased cell type identification
329 from single-cell RNA sequencing data. Subsequently, specific highly-expressed genes
330 were combined with those derived from review of the literature for manual annotation
331 to ultimately determine cell types. Classic biomarkers for specific cell types were used
332 to identify cells in different clusters.

333 **Differential Gene Identification and Functional Analysis**

334 The *FindMarkers()* function in the Seurat package was used to identify DEGs
335 between different cell groups, with criteria of |log2FC| > 0.25 and p-value<0.05,
336 pct.1>0.25. The ClusterProfiler R package was utilized for GO, KEGG, and GSEA
337 enrichment analyses, and the ggplot2 and enrichplot R packages were used for
338 visualization.

339 **Measurement of HTNV specific antibodies**

340 Levels of serum IgM and IgG antibodies to HTNV NP were assessed through the
341 enzyme-linked immunosorbent assay (ELISA) kit (Wantai BioPharm, Beijing, China)
342 in accordance with the manufacturer's instructions.

343 **Analysis of IgG glycans**

344 The process of isolating, labelling, purifying, and analyzing plasma IgG was
345 performed using previously established methods (Hou et al., 2019; Pengcheng Liu,
346 2023). Briefly, the diluted plasma samples were transferred onto a 96-well protein G
347 monolithic plate (BIA Separations, Slovenia) for the isolation of IgG. The isolated IgG
348 was eluted with 1 mL of 0.1 M formic acid and was immediately neutralized with 170
349 μL of 1M ammonium bicarbonate.

350 The released N-glycans were labelled with 2-aminobenzamide (2-AB) and were then
351 purified from a mixture of 100% acetonitrile and ultrapure water in a 1:1 ratio (v/v).
352 This was then analyzed by hydrophilic interaction liquid chromatography using ultra-
353 performance liquid chromatography (HILIC-UPLC; Walters Corporation, Milford, MA)
354 (Hou et al., 2019). As previously reported, the chromatograms were separated into 24
355 IgG glycan peaks (GPs) (Menni et al., 2018).

356 Our study incorporated both biological and technical replicates to ensure a robust
357 glycomic profiling analysis. Specifically, we analyzed paired acute/convalescent-phase

358 samples from 65 confirmed HFRS patients to assess inter-individual biological
359 variability, while technical reproducibility was validated through comparison with
360 standard chromatographic peak plots (Vučković et al., 2016). This dual-replicate
361 strategy enabled a comprehensive evaluation of both biological heterogeneity and assay
362 precision, and the coefficient of variation for samples were below 16%.

363 **Virus-specific B-cell detection**

364 Virus-specific B-cell against HTNV were performed as previously described (Liechti
365 & Roederer, 2019; Song et al., 2018). All antibodies used for flow cytometry were
366 purchased from BioLegend or BD Biosciences. Antibody combination was as follows:
367 CD3-FITC (cat, 300406), CD19-PerCP-Cy5.5 (cat, 561295), CD21-APC (cat, 559867),
368 CD27-DAPI (cat, 562513), CD38-PE (cat, 555460), IgD-Amcyan (cat, 563034), IgG-
369 PE-CY7 (cat, 561298), and IgM-BV605 (cat, 562977).

370 **Statistical analysis**

371 Categorical variables were compared using chi-square tests. Normality of numeric
372 variables was assessed with the Kolmogorov-Smirnov test; non-normally distributed
373 continuous variables were analyzed using non-parametric tests. The Benjamini -
374 Hochberg (BH) method was used to adjust the raw p-values from DEG analysis,
375 controlling the false discovery rate (FDR). Statistical analyses were performed with R
376 software version 4.1.1 (R Core Team, New Zealand) and GraphPad Prism 8 (GraphPad
377 Software, San Diego, CA), with a significance level of $\alpha = 0.05$ (two-tailed).

378 **Funding**

Funder	Grant reference number	Author
the Natural Science Foundation of Shandong Province	Grant numbers ZR2020QH133	Chuansong Quan
the Natural Science Foundation of Shandong Province	Grant numbers ZR2022MH082	Haifeng Hou

the Natural Science Foundation of Shandong Province	Grant numbers ZR2024MH235	Weijia Xing
the Natural Science Foundation of Shandong Province	Grant numbers ZR201911090028	Yaoni Li
Shaanxi Provincial Natural Science Basic Research Program of Shaanxi Province	Grant number 2023-JC-YB-741	Yaoni Li

Data availability

The raw RNAseq data used for this study is available at the BioProject database (the accession number: PRJNA1238574) under the digital object identifier: https://www.ncbi.nlm.nih.gov/bioproject/PRJNA1238574.

The following datasets were reanalysed:

Zhang H, Wang Y (2022) Increased CD4+CD8+ double positive T cells during Hantaan virus infection ID GSE161354. In the public domain at GEO https://www.ncbi.nlm.nih.gov/geo/query/acc.cgi?acc=GSE161354.

Zheng Y, Liu X (2020) A human circulating immune cell landscape in aging and COVID-19 ID HRA000203. In the public domain at GSA https://ngdc.cncb.ac.cn/gsa-human/browse/HRA000203.

Disclosure statement

No potential conflict of interest was reported by the author(s).

References

Zheng, Z., Wang, P., Wang, Z., Zhang, D., Wang, X., Zuo, S., & Li, X. (2019). The characteristics of current natural foci of hemorrhagic fever with renal syndrome in Shandong Province, China, 2012-2015. PLoS Negl Trop Dis, 13(5), e0007148. doi:10.1371/journal.pntd.0007148

Li, R., Sun, J., Chen, Y., Fan, X., Wang, X., Zhang, X., . . . Liu, Z. (2023). Clinical and laboratory features and factors predicting disease severity in pediatric patients with hemorrhagic fever with renal syndrome caused by Hantaan virus. J Med Virol, 95(1), e28339. doi:10.1002/jmv.28339

Pizarro, E., Navarrete, M., Mendez, C., Zaror, L., Mansilla, C., Tapia, M., . . . Rodríguez, E. M. (2019). Immunocytochemical and ultrastructural evidence supporting that Andes Hantavirus (ANDV) is transmitted person-to-person through the respiratory and/or salivary pathways. Front Microbiol, 10, 2992. doi:10.3389/fmicb.2019.02992

Tariq, M., & Kim, D. M. (2022). Hemorrhagic fever with renal syndrome: literature review, epidemiology, clinical picture and pathogenesis. Infect Chemother, 54(1), 1–19. doi:10.3947/ic.2021.0148

Engdahl, T. B., & Crowe, J. E., Jr. (2020). Humoral immunity to Hantavirus infection. mSphere, 5(4). doi:10.1128/mSphere.00482-20

Li, Y., Quan, C., Xing, W., Wang, P., Gao, J., Zhang, Z., . . . Shi, W. (2020). Rapid humoral immune responses are required for recovery from haemorrhagic fever with renal syndrome patients. Emerg Microbes Infect, 9(1), 2303–2314. doi:10.1080/22221751.2020.1830717

Ash, M. K., Bhimalli, P. P., Cho, B. K., Mattamana, B. B., Gambut, S., Tarhoni, I., . . . Schneider, J. R. (2022). Bulk IgG glycosylation predicts COVID-19 severity and vaccine antibody response. Cell Rep, 41(11), 111799.

417 doi:10.1016/j.celrep.2022.111799

418 Haslund-Gourley, B. S., Woloszczuk, K., Hou, J., Connors, J., Cusimano, G., Bell,
419 M., . . . Comunale, M. A. (2024). IgM N-glycosylation correlates with COVID-19
420 severity and rate of complement deposition. Nat Commun, 15(1), 404.
421 doi:10.1038/s41467-023-44211-0

422 Hou, H., Yang, H., Liu, P., Huang, C., Wang, M., Li, Y., . . . Wang, W. (2021). Profile
423 of immunoglobulin G N-glycome in COVID-19 patients: a case-control study. Front
424 Immunol, 12, 748566. doi:10.3389/fimmu.2021.748566

425 Wang, T. T., Sewatanon, J., Memoli, M. J., Wrammert, J., Bournazos, S., Bhaumik,
426 S. K., . . . Ravetch, J. V. (2017). IgG antibodies to dengue enhanced for FcγRIIIA
427 binding determine disease severity. Science, 355(6323), 395–398.
428 doi:10.1126/science.aai8128

429 Onwuchekwa, C., Moreo, L. M., Menon, S., Machado, B., Curcio, D., Kalina, W., . . .
430 Begier, E. (2023). Underascertainment of respiratory syncytial virus infection in adults
431 due to diagnostic testing limitations: a systematic literature review and meta-analysis.
432 J Infect Dis, 228(2), 173–184. doi:10.1093/infdis/jiad012

433 Larsen, M. D., de Graaf, E. L., Sonneveld, M. E., Plomp, H. R., Nouta, J., Hoepel,
434 W., . . . Vidarsson, G. (2021). Afucosylated IgG characterizes enveloped viral responses
435 and correlates with COVID-19 severity. Science, 371(6532).
436 doi:10.1126/science.abc8378

437 Lu, L. L., Suscovich, T. J., Fortune, S. M., & Alter, G. (2018). Beyond binding:
438 antibody effector functions in infectious diseases. Nat Rev Immunol, 18(1), 46–61.
439 doi:10.1038/nri.2017.106

440 Wieczorek, M., Braicu, E. I., Oliveira-Ferrer, L., Sehouli, J., & Blanchard, V. (2020).
441 Immunoglobulin G subclass-specific glycosylation changes in primary epithelial

ovarian cancer. Front Immunol, 11, 654. doi:10.3389/fimmu.2020.00654

Giron, L. B., Colomb, F., Papasavvas, E., Azzoni, L., Yin, X., Fair, M., . . . Abdel-Mohsen, M. (2020). Interferon-α alters host glycosylation machinery during treated HIV infection. EBioMedicine, 59, 102945. doi:10.1016/j.ebiom.2020.102945

Irvine, E. B., & Alter, G. (2020). Understanding the role of antibody glycosylation through the lens of severe viral and bacterial diseases. Glycobiology, 30(4), 241–253. doi:10.1093/glycob/cwaa018

Ackerman, M. E., Das, J., Pittala, S., Broge, T., Linde, C., Suscovich, T. J., . . . Alter, G. (2018). Route of immunization defines multiple mechanisms of vaccine-mediated protection against SIV. Nat Med, 24(10), 1590–1598. doi:10.1038/s41591-018-0161-0

Jennewein, M. F., & Alter, G. (2017). The immunoregulatory roles of antibody glycosylation. Trends Immunol, 38(5), 358–372. doi:10.1016/j.it.2017.02.004

Liu, D., Chu, X., Wang, H., Dong, J., Ge, S. Q., Zhao, Z. Y., . . . Wang, W. (2018). The changes of immunoglobulin G N-glycosylation in blood lipids and dyslipidaemia. J Transl Med, 16(1), 235. doi:10.1186/s12967-018-1616-2

Houde, D., Peng, Y., Berkowitz, S. A., & Engen, J. R. (2010). Post-translational modifications differentially affect IgG1 conformation and receptor binding. Mol Cell Proteomics, 9(8), 1716–1728. doi:10.1074/mcp.M900540-MCP200

Hwang, H. J., Kang, D., Shin, J., Jung, J., Ko, S., Jung, K. H., . . . Lee, J. S. (2025). Therapy-induced senescent cancer cells contribute to cancer progression by promoting ribophorin 1-dependent PD-L1 upregulation. Nat Commun, 16(1), 353. doi:10.1038/s41467-024-54132-1

Wang, T. T., & Ravetch, J. V. (2019). Functional diversification of IgGs through Fc glycosylation. J Clin Invest, 129(9), 3492–3498. doi:10.1172/jci130029

Yang, Z., Wang, S., Halim, A., Schulz, M. A., Frodin, M., Rahman, S. H., . . . Clausen,

H. (2015). Engineered CHO cells for production of diverse, homogeneous glycoproteins. Nat Biotechnol, 33(8), 842–844. doi:10.1038/nbt.3280

Ma, Y., Yuan, B., Zhuang, R., Zhang, Y., Liu, B., Zhang, C., . . . Jin, B. (2015). Hantaan virus infection induces both Th1 and ThGranzyme B+ cell immune responses that associated with viral control and clinical outcome in humans. PLoS Pathog, 11(4), e1004788. doi:10.1371/journal.ppat.1004788

Tang, K., Zhang, C., Zhang, Y., Zhang, Y., Du, H., Jin, B., & Ma, Y. (2019). Elevated plasma interleukin 34 levels correlate with disease severity-reflecting parameters of patients with haemorrhagic fever with renal syndrome. Infect Dis (Lond), 51(11-12), 847–853. doi:10.1080/23744235.2019.1672887

Zhang, H., Wang, Y., Ma, Y., Tang, K., Zhang, C., Wang, M., . . . Zhang, Y. (2022). Increased CD4(+)CD8(+) double positive T cells during Hantaan virus infection. Viruses, 14(10). doi:10.3390/v14102243

Chakraborty, S., Gonzalez, J. C., Sievers, B. L., Mallajosyula, V., Chakraborty, S., Dubey, M., . . . Wang, T. T. (2022). Early non-neutralizing, afucosylated antibody responses are associated with COVID-19 severity. Sci Transl Med, 14(635), eabm7853. doi:10.1126/scitranslmed.abm7853

Jin, C., Chen, Y., Wang, Y., Li, J., Liang, J., Zheng, S., . . . Yang, H. (2024). Single-cell RNA sequencing reveals special basal cells and fibroblasts in idiopathic pulmonary fibrosis. Sci Rep, 14(1), 15778. doi:10.1038/s41598-024-66947-5

Hou, H., Xu, X., Sun, F., Zhang, X., Dong, H., Wang, L., . . . Wang, Y. (2019). Hyperuricemia is associated with immunoglobulin G N-glycosylation: a community-based study of glycan biomarkers. Omics, 23(12), 660–667. doi:10.1089/omi.2019.0004

Pengcheng Liu, X. W., Aishe Dun, Yutong Li, Houqiang Li, Lu Wang, Yichun Zhang,

Cancan Li, Jinxia Zhang, Xiaoyu Zhang, Lixing Ma f, Haifeng Hou. (2023). High-throughput profiling of serological immunoglobulin G N-glycome as a noninvasive biomarker of gastrointestinal cancers. Engineering, 26(7), 44–53. doi:10.1016/j.eng.2023.02.008

Menni, C., Gudelj, I., Macdonald-Dunlop, E., Mangino, M., Zierer, J., Bešić, E., . . . Valdes, A. M. (2018). Glycosylation profile of immunoglobulin G is cross-sectionally associated with cardiovascular disease risk score and subclinical atherosclerosis in two independent cohorts. Circ Res, 122(11), 1555–1564. doi:10.1161/circresaha.117.312174

Vučković, F., Theodoratou, E., Thaçi, K., Timofeeva, M., Vojta, A., Štambuk, J., . . . Lauc, G. (2016). IgG glycome in colorectal cancer. Clin Cancer Res, 22(12), 3078–3086. doi:10.1158/1078-0432.Ccr-15-1867

Liechti, T., & Roederer, M. (2019). OMIP-051 - 28-color flow cytometry panel to characterize B cells and myeloid cells. Cytometry A, 95(2), 150–155. doi:10.1002/cyto.a.23689

Song, P., Zheng, N., Liu, Y., Tian, C., Wu, X., Ma, X., . . . Wu, Z. (2018). Deficient humoral responses and disrupted B-cell immunity are associated with fatal SFTSV infection. Nat Commun, 9(1), 3328. doi:10.1038/s41467-018-05746-9

510 **Figure legends**

511 **Figure 1. Flow chart of HFRS patient recruitment in Baoji Central Hospital in**
512 **Shaanxi province from November 2019 to January 2022.**

513 **Figure 2. Immunophenotypic remodeling in the B-cell subsets during acute HFRS.**
514 (A) t-distributed stochastic neighbor embedding (t-SNE) plot showing antibody
515 secreting memory B cells (ASM), double negative (DN) B cells, intermediate memory
516 cells (IM), marginal zone-like cells (MZB), naive B cells, plasmablasts (PB), quiescent
517 resting memory cells (RM), and exhausted tissue-like memory B cells (TLM) of
518 PBMCs identified using an integrated and classification analysis. (B) t-SNE projection
519 of canonical markers, including CD19, CD27, CD38, IgD, and IgM. (C) Proportions of
520 the eight B cell subsets, colored by the healthy group (green) and HTNV groups (red).
521 Boxplot features: minimum box, 25th percentile; center, median; maximum box, 75th
522 percentile. (D) Frequency of the eight B cell subsets in between the healthy group (n =
523 8) and HTNV groups (n = 15). (E) FACS gating strategy for the measurement of the B-
524 cell subsets: activated memory B cells ($CD21^-$ $CD27^+$, AM), RM B cells ($CD21^+$
525 $CD27^+$), IM B cells ($CD21^+$ $CD27^-$), TLM B cells ($CD21^-$ $CD27^-$), naive B cells ($CD27^-$
526 IgD^+), MZB B cells ($CD27^+$ IgD^+), ASM B cells ($CD27^+$ IgD^-), DN B cells ($CD27^-$ IgD^-),
527 PB ($CD38^+$ $CD27^+$), and class-switched memory B cells ($CD38^-$ $CD27^+$, CSM),
528 respectively. (F) The proportion of ASM, CSM, naive B, and PB cells in $CD19^+$ B cells
529 in the acute and convalescent HFRS patients. Data are presented as mean ± SEM in
530 panels C and F. *$p<0.05$ (Student's t-test).

531 **Figure 3. Glycosylation modification of antibodies associated with HTNV infection.**
532 (A) Changes of different glycosylation types in both HTNV NP-specific IgG negative
533 and positive plasma from 24 HFRS patients. (B) Differential IgG glycosylation patterns
534 across antibody titer levels quantified by ELISA. (C) Comparison of different

535 glycosylation levels before and after the fourfold increase in the IgG antibody titers.
536 *p<0.05, **p<0.01, ***p<0.001. For paired samples, Wilcoxon Signed Rank Test was
537 used to assess the difference.

538 **Figure 4. Glycosylation modifications of antibodies primarily deprived from**
539 **antibody-secreting and plasmablast subpopulations.**

540 (A) The correlation between the proportion of PB cells and the sialylation level. (B)
541 The correlation between the proportion of ASM cells and the sialylation level. (C) The
542 correlation between the proportion of ASM cells and the galactosylation level. (D) Dot
543 plot shows the expression levels of glycosylation-related genes in the eight B cell
544 groups. The pink color represents mannose related genes, the green color represents N-
545 glycosylation-related genes, the orange color represents galactosylation-related genes,
546 the purple represents sialylation-related genes, and the red color represents fucosylation
547 related genes. (E) Enriched pathways in the plasmablast and ASM subsets by GO
548 enrichment analysis of the DEGs. (F) The GSEA map presents the enrichment score of
549 GRGs in N-Glycan biosynthesis.

550 **Supplementary materials**

551 **Supplementary file 1. The proportion of different B cell subpopulations between**
552 **healthy and acute HFRS groups.**

553 **Supplementary file 2. Difference in main IgG glycome features of HFRS patients**
554 **between age groups.**

555 **Supplementary file 3. Difference in main IgG glycome features of HFRS patients**
556 **between sex groups.**

557 **Supplementary file 4. Relative abundance (%) of the main IgG-Fc glycome**
558 **features in HFRS patients.**

559 **Supplementary file 5. Results of multiple linear regression analysis**
560 **for fucosylation.**

561 APTT, activated partial thromboplastin time; MCHC, mean corpuscular hemoglobin
562 concentration; NEUT, neutrophil; PLT, platelet; WBC, white blood cell; CRE,
563 creatinine; Cys-C, cystatin C.

564 **Supplementary file 6. Results of multiple linear regression analysis for bisecting**
565 **GlcNAc.**

566 APTT, activated partial thromboplastin time; MCHC, mean corpuscular hemoglobin
567 concentration; NEUT, neutrophil; PLT, platelet; WBC, white blood cell; CRE,
568 creatinine; Cys-C, cystatin C.

569 **Supplementary file 7. Results of multiple linear regression analysis**
570 **for galactosylation.**

571 APTT, activated partial thromboplastin time; MCHC, mean corpuscular hemoglobin
572 concentration; NEUT, neutrophil; PLT, platelet; WBC, white blood cell; CRE,
573 creatinine; Cys-C, cystatin C.

574 **Supplementary file 8. Results of multiple linear regression analysis for sialylation.**

575 APTT, activated partial thromboplastin time; MCHC, mean corpuscular hemoglobin
576 concentration; NEUT, neutrophil; PLT, platelet; WBC, white blood cell; CRE,
577 creatinine; Cys-C, cystatin C.

578 **Supplementary file 9. Differentially expressed genes among different B cell**
579 **subgroups in healthy and acute HFRS groups.**

580 **Supplementary file 10. Differential expression genes in the ASM, PB and RM B**
581 **cell subpopulations.**

582 **Supplementary file 11. Differential expression genes in the DN, IM and naive B**
583 **cell subpopulations.**

584

585 **Figure 2—figure supplement 1. Single-cell transcriptomes of PBMCs from**
586 **patients with HFRS.**

587 (A) Uniform manifold approximation and projection (UMAP) presentation of the major
588 peripheral immune cell types in the PBMCs from 15 HFRS patients and 8 healthy
589 controls. (B) Dot plot shows the expression levels of canonical marker-related genes in
590 the different subpopulations. (C) UMAP presentation of the major peripheral immune
591 cell types among HFRS and healthy control groups. (D) Proportions of the eight cell
592 subsets, colored by the healthy group (green) and HTNV groups (red). Boxplot features:
593 minimum box, 25th percentile; center, median; maximum box, 75th percentile. (E)
594 Frequency of the eight cell subsets in between the healthy group (n = 8) and the HTNV
595 group (n = 15). (F) The UMAP plot shows the differentiation trajectories of different
596 cell types calculated by pseudotime analysis.

597 **Figure 2—figure supplement 2. Dynamic analysis of the B-cell subsets in HFRS**
598 **patients.**

599 (A) Expression of MZB in $CD19^+$ B cells. (B) Expression of DN in $CD19^+$ B cells. (C)

600 Expression of TLM in $CD19^+$ B cells. (D) Expression of AM in $CD19^+$ B cells. (E)
601 Expression of RM in $CD19^+$ B cells. (F) Expression of IM in $CD19^+$ B cells.

602 **Figure 4—figure supplement 1. The differentially expressed genes and their**
603 **functional changes in the B cell subsets post HTNV infection.**

604 (A) The volcano plot shows the differentially expressed genes of different B cell subsets
605 in acute HFRS patients. The red font represents the upregulation of the B cell
606 subpopulations, and the blue font represents the downregulation of the B cell
607 subpopulations. (B and C) The volcano plot displays the differentially expressed genes
608 in upregulation B cell subpopulations including antibody secreting memory B cells,
609 plasmablasts, and quiescent resting memory B cells (B), and downregulation B cell
610 subpopulations including naive B cells, double negative B cells, and intermediate
611 memory B cells (C).

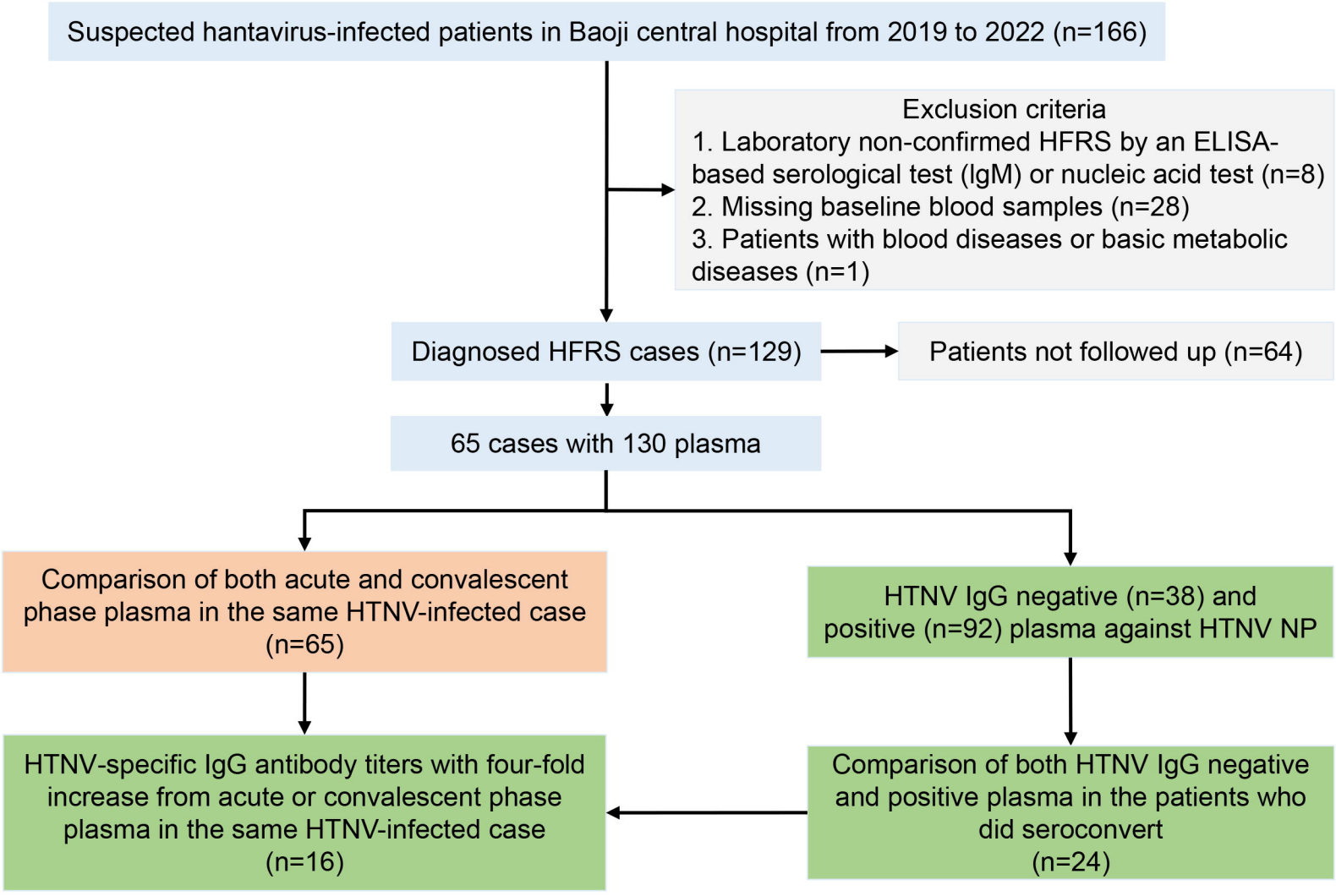
Suspected hantavirus-infected patients in Baoji central hospital from 2019 to 2022 (n=166)
Exclusion criteria
1. Laboratory non-confirmed HFRS by an ELISA-based serological test (IgM) or nucleic acid test (n=8)
2. Missing baseline blood samples (n=28)
3. Patients with blood diseases or basic metabolic diseases (n=1)
Diagnosed HFRS cases (n=129)
Patients not followed up (n=64)
65 cases with 130 plasma
Comparison of both acute and convalescent phase plasma in the same HTNV-infected case (n=65)
HTNV IgG negative (n=38) and positive (n=92) plasma against HTNV NP
HTNV-specific IgG antibody titers with four-fold increase from acute or convalescent phase plasma in the same HTNV-infected case (n=16)
Comparison of both HTNV IgG negative and positive plasma in the patients who did seroconvert (n=24)

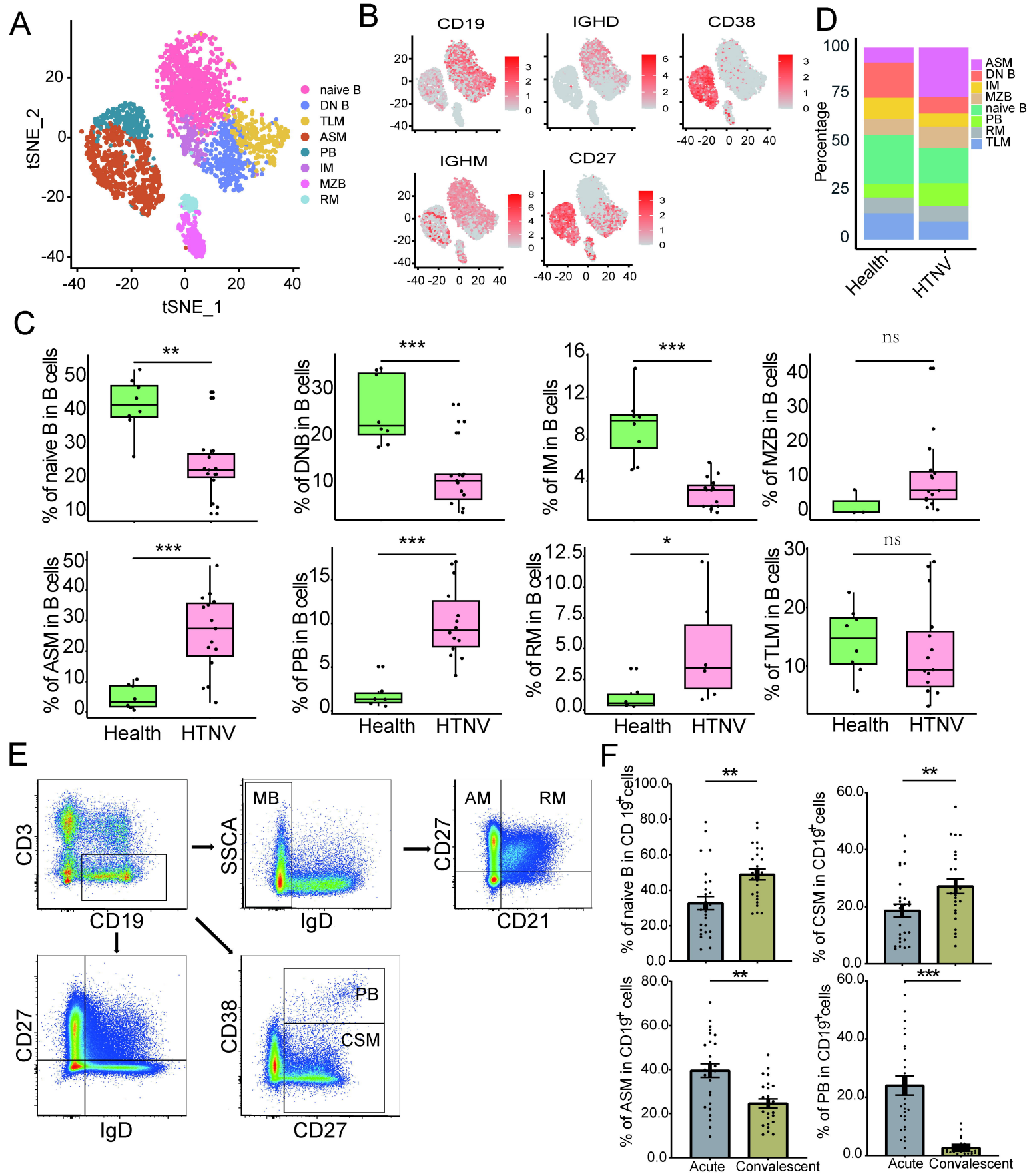
A
tSNE_2
tSNE_1
naive B
DN B
TLM
ASM
PB
IM
MZB
RM
B
CD19
IGHD
CD38
IGHM
CD27
D
Percentage
Health
HTNV
C
% of naive B in B cells
% of DNB in B cells
% of IM in B cells
% of MZB in B cells
% of ASM in B cells
% of PB in B cells
% of RM in B cells
% of TLM in B cells
ns
E
CD3
CD19
SSCA
MB
IgD
CD27
AM
RM
CD21
PB
CSM
CD38
F
% of naive B in CD 19+cells
% of CSM in CD19+cells
% of ASM in CD19+ cells
% of PB in CD19+cells
Acute
Convalescent

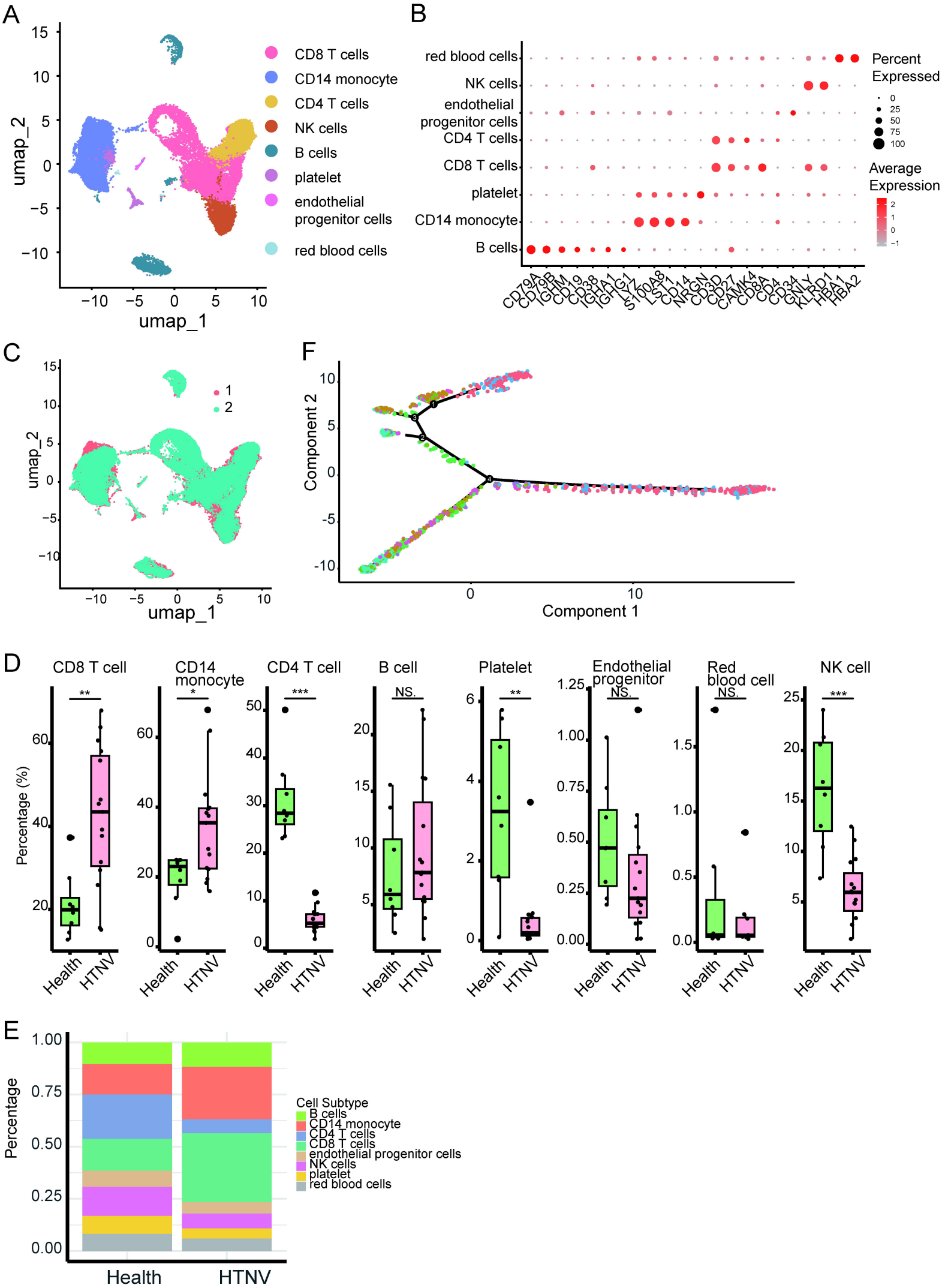
A
umap_2
umap_1
CD8 T cells
CD14 monocyte
CD4 T cells
NK cells
B cells
platelet
endothelial progenitor cells
red blood cells
B
Percent Expressed
Average Expression
CD79A
CD79B
IGHM
CD19
CD38
IGHA1
IGHG1
LYZ
S100A8
LST1
CD14
NRGN
CD3D
CD27
CAMK4
CD8A
CD4
CD34
GNLY
KLRD1
HBA1
HBA2
C
F
Component 1
Component 2
D
CD8 T cell
CD14 monocyte
CD4 T cell
B cell
Platelet
Endothelial progenitor
Red blood cell
NK cell
Percentage (%)
Health
HTNV
E
Percentage
Cell Subtype
B cells
CD14 monocyte
CD4 T cells
CD8 T cells
endothelial progenitor cells
NK cells
platelet
red blood cells

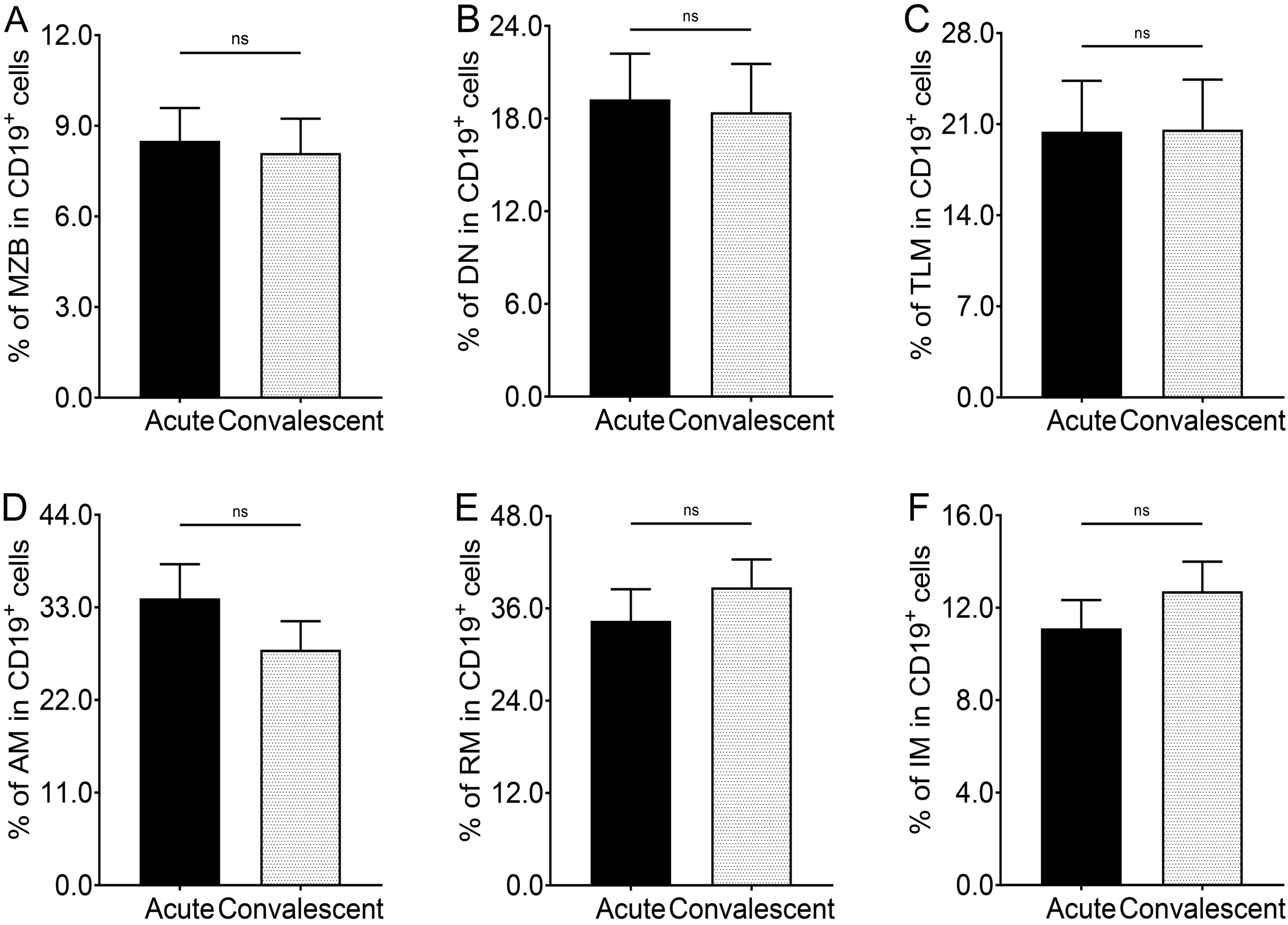
A
% of MZB in CD19+ cells
12.0
9.0
6.0
3.0
0.0
ns
Acute
Convalescent
B
% of DN in CD19+ cells
24.0
18.0
12.0
6.0
0.0
ns
Acute
Convalescent
C
% of TLM in CD19+ cells
28.0
21.0
14.0
7.0
0.0
ns
Acute
Convalescent
D
% of AM in CD19+ cells
44.0
33.0
22.0
11.0
0.0
ns
Acute
Convalescent
E
% of RM in CD19+ cells
48.0
36.0
24.0
12.0
0.0
ns
Acute
Convalescent
F
% of IM in CD19+ cells
16.0
12.0
8.0
4.0
0.0
ns
Acute
Convalescent

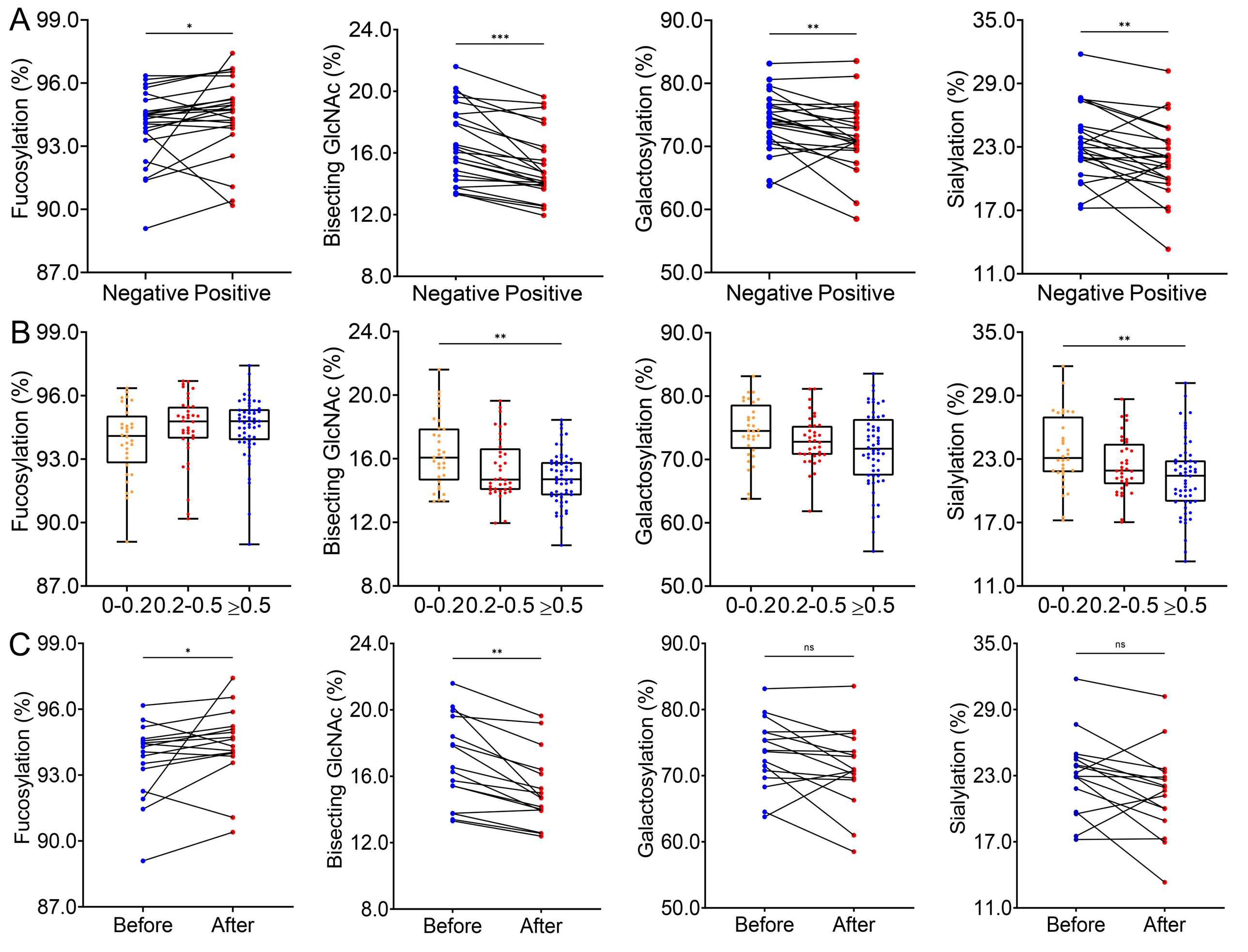
A
Fucosylation (%)
99.0
96.0
93.0
90.0
87.0
*
Negative Positive
Bisecting GlcNAc (%)
24.0
20.0
16.0
12.0
8.0
***
Negative Positive
Galactosylation (%)
90.0
80.0
70.0
60.0
50.0
**
Negative Positive
Sialylation (%)
35.0
29.0
23.0
17.0
11.0
**
Negative Positive
B
Fucosylation (%)
99.0
96.0
93.0
90.0
87.0
0-0.2 0.2-0.5 ≥0.5
Bisecting GlcNAc (%)
24.0
20.0
16.0
12.0
8.0
**
0-0.2 0.2-0.5 ≥0.5
Galactosylation (%)
90.0
80.0
70.0
60.0
50.0
0-0.2 0.2-0.5 ≥0.5
Sialylation (%)
35.0
29.0
23.0
17.0
11.0
**
0-0.2 0.2-0.5 ≥0.5
C
Fucosylation (%)
99.0
96.0
93.0
90.0
87.0
*
Before After
Bisecting GlcNAc (%)
24.0
20.0
16.0
12.0
8.0
**
Before After
Galactosylation (%)
90.0
80.0
70.0
60.0
50.0
ns
Before After
Sialylation (%)
35.0
29.0
23.0
17.0
11.0
ns
Before After

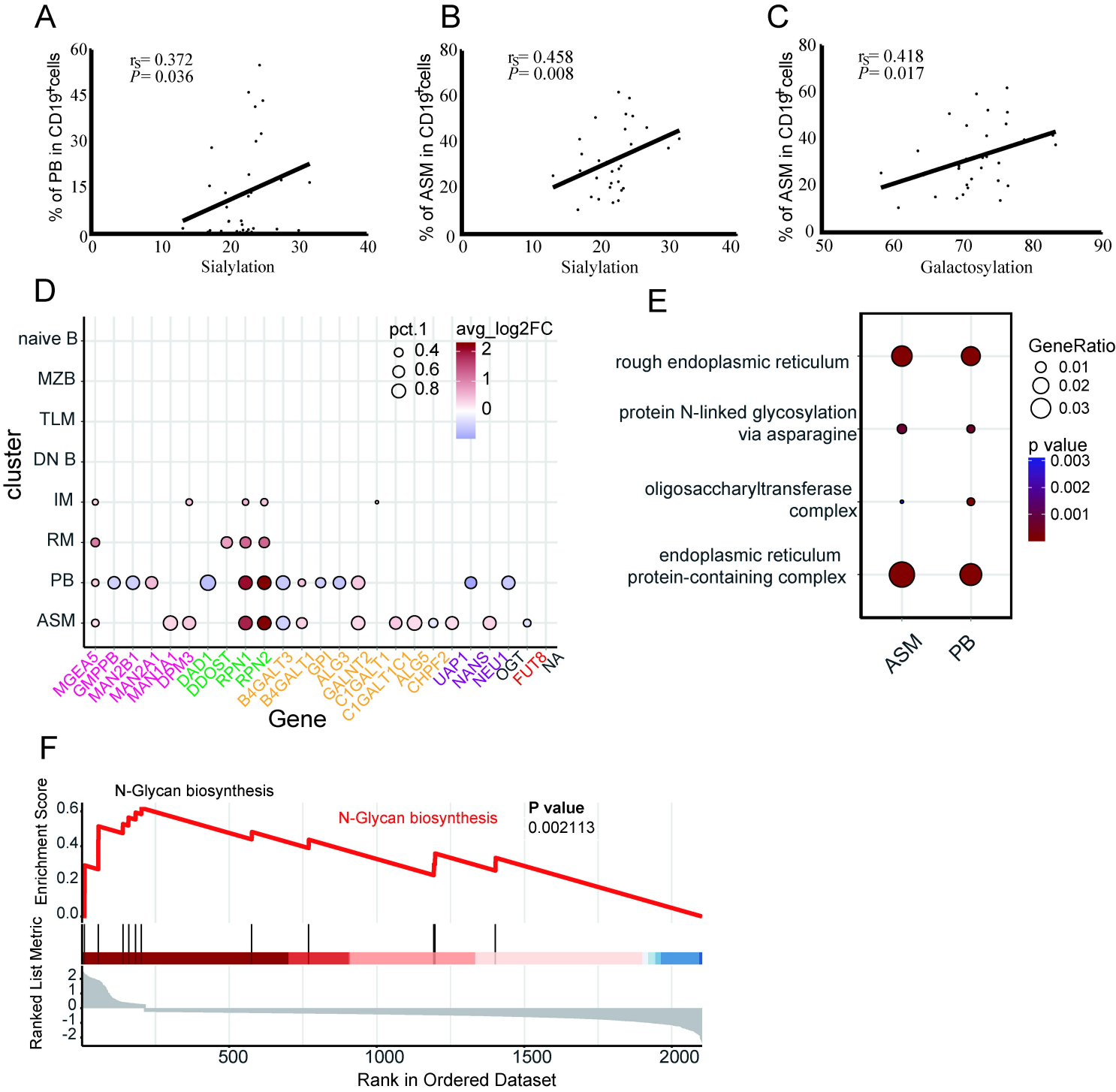
A
% of PB in CD1g+cells
rs= 0.372
P= 0.036
Sialylation
B
% of ASM in CD1g+cells
rs= 0.458
P= 0.008
Sialylation
C
% of ASM in CD1g+cells
rs= 0.418
P= 0.017
Galactosylation
D
naive B
MZB
TLM
DN B
IM
RM
PB
ASM
cluster
pct.1
0.4
0.6
0.8
avg_log2FC
2
1
0
MGEA5
GMPPB
MAN2B1
MAN2A1
MAN1A1
DPM3
PAD1
DDOST
RPN1
RPN2
B4GALT3
B4GALT1
GPI
ALG3
GALNT2
C1GALT1
C1GALT1C1
ALG5
CHPF2
UAP1
NANS
NEU1
OGT
FUT8
NA
Gene
E
rough endoplasmic reticulum
protein N-linked glycosylation via asparagine
oligosaccharyltransferase complex
endoplasmic reticulum protein-containing complex
ASM
PB
GeneRatio
0.01
0.02
0.03
p value
0.003
0.002
0.001
F
N-Glycan biosynthesis
Enrichment Score
N-Glycan biosynthesis
P value
0.002113
Ranked List Metric
Rank in Ordered Dataset

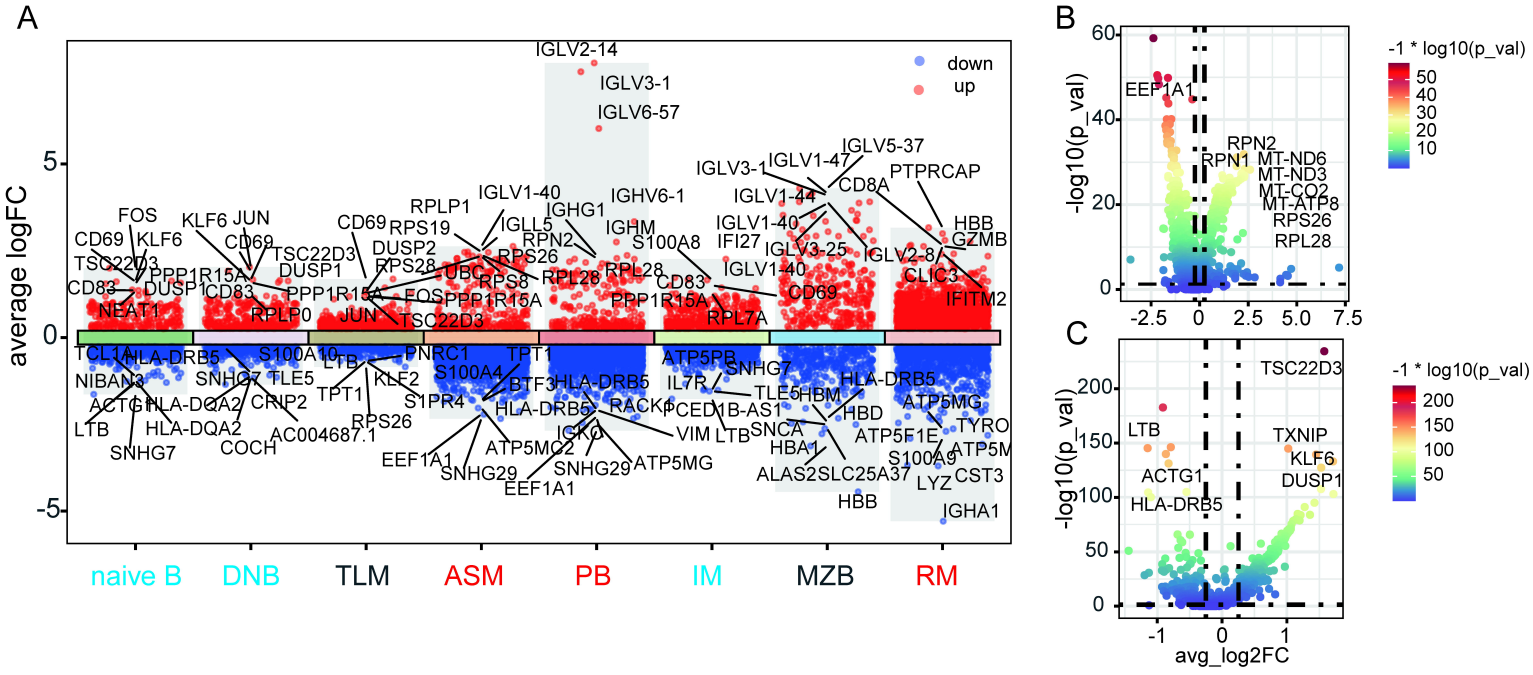
A
average logFC
down
up
naive B
DNB
TLM
ASM
PB
IM
MZB
RM
B
-log10(p_val)
-1 * log10(p_val)
EEF1A1
RPN2
RPN1
MT-ND6
MT-ND3
MT-CO2
MT-ATP8
RPS26
RPL28
C
-log10(p_val)
avg_log2FC
-1 * log10(p_val)
TSC22D3
LTB
TXNIP
KLF6
DUSP1
ACTG1
HLA-DRB5